Additive Manufacturing: Metallurgy, Cut Analysis & Porosity

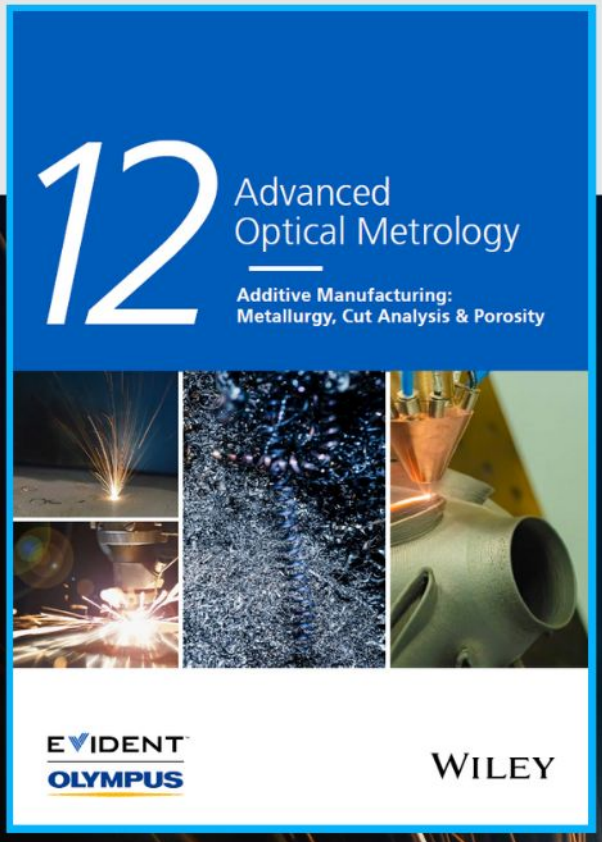

The latest eBook from Advanced Optical Metrology. Download for free.

In industry, sector after sector is moving away from conventional production methods to additive manufacturing, a technology that has been recommended for substantial research investment.

Download the latest eBook to read about the applications, trends, opportunities, and challenges around this process, and how it has been adapted to different industrial sectors.

EVIDENT
OLYMPUS

WILEY

ADVANCED FUNCTIONAL MATERIALS
www.afm-journal.de

Segregated and Non-Settling Liquid Metal Elastomer via Jamming of Elastomeric Particles

Xiaoting Xue, Dongguang Zhang, Yali Wu,* Ruizhe Xing, Hong Li, Tingting Yu, Bowen Bai, Yebo Tao, Michael D. Dickey, and Jiayi Yang**

Liquid metal elastomer (LME)—that is, liquid metal particles dispersed in elastomer—is a soft material that has useful electric, dielectric, and thermal properties. Two issues with LME are sought to be addressed: 1) the dense liquid metal (LM) particles can settle before curing of the elastomer, and 2) the LM particles are separated by a thin layer of insulating elastomer and therefore require some "mechanical sintering" to break this layer to create conductive paths. These issues are addressed using an LME containing elastic particles (LMEP). Elastic polydimethylsiloxane particles (PPs) and LM particles jam to prevent particle settling. Meanwhile, the PPs reduce the loading necessary to create conductive paths, thus decreasing the density and cost relative to LME. Surprisingly, the particles percolate into conductive paths prior to curing the LMEP but not in LME. The dielectric constant, electrical conductivity, and thermal conductivity of LMEPs are investigated by changing the volume fraction of LM particles, polydimethylsiloxane prepolymer and PPs, and propose an LMEP with the optimal ratio. In addition, LMEP-based sensors and circuits are demonstrated for wearable electronics.

1. Introduction

Gallium-based liquid metals (LMs) have been extensively studied due to their low melting point (15.5 °C), high electrical conductivity (3.5×10^6 S m^{-1}), high thermal conductivity (14 W m^{-1} K), and non-toxicity.[1] Mixing bulk LMs with elastomers (e.g., polydimethylsiloxane) forms liquid metal elastomers (LMEs) with high thermal and electrical conductivity, elevated dielectric constant, and increased toughness.[2] LME can be used to fabricate sensors,[3] self-healing conductors,[4] shape-memory materials,[5] thermoelectric devices,[6] and has great application potential in soft robots,[7] wearable devices,[8] and human-machine interfaces.[9]

The curing process of LMEs can take several hours. During the casting and curing process, LM particles settle due to their density which is approximately seven times that of elastomers. Some works have intentionally prepared LM particle rich regions by extending the curing time of LMEs to self-encapsulate conductors or create shape memory composites.[10] On the contrary, for the applications of LME as dielectrics, electrical and thermal conductors, the settled LM particles lower the effective dielectric constant as well as the electrical and thermal conductivity of LME.[10b,11] Therefore, adding a higher volume ratio of LMs is needed to achieve the desired performance, which increases the weight and cost. At extreme loadings, it can lead to leakage. Notably, the settlement of LM particles occurs before curing. The settling can be alleviated by changing the thickness, especially for applications such as 3D printing composites in which curing is done after printing.[12] However, when increasing the sample height or decreasing the LM volume fraction, the settling phenomenon still exists.[10b]

Doping LMEs with nanoparticles,[13] nanoplatelets,[14] nanotubes,[15] or light particles[16] improves the dielectric constant, electrical, and thermal conductivity of LMEs. Such additives can bridge between LM particles to form electrical and

X. Xue, D. Zhang, Y. Wu
College of Mechanical and Vehicle Engineering
Taiyuan University of Technology
Taiyuan 030024, P. R. China
E-mail: zhangdongguang@tyut.edu.cn; wuyali@tyut.edu.cn

R. Xing
School of Chemistry and Chemical Engineering
Northwestern Polytechnical University
Xi'an 710072, P. R. China

H. Li
Shanxi TZ Digitization & Intelligence Technology Co., LTD
Taiyuan 030000, P. R. China

The ORCID identification number(s) for the author(s) of this article can be found under https://doi.org/10.1002/adfm.202210553.

DOI: 10.1002/adfm.202210553

T. Yu, B. Bai
School of Aerospace Science and Technology
Xidian University
Xi'an 710071, P. R. China

Y. Tao
Intelligent manufacturing College
Jiaxing Vocational & Technical College
Jiaxing 314036, P. R. China

M. D. Dickey
Department of Chemical and Biomolecular Engineering
North Carolina State University
Raleigh, NC 27695, USA

J. Yang
College of Computer Science and Technology
Xi'an University of Science and Technology
Xi'an 710054, P. R. China
E-mail: jyang46@xust.edu.cn

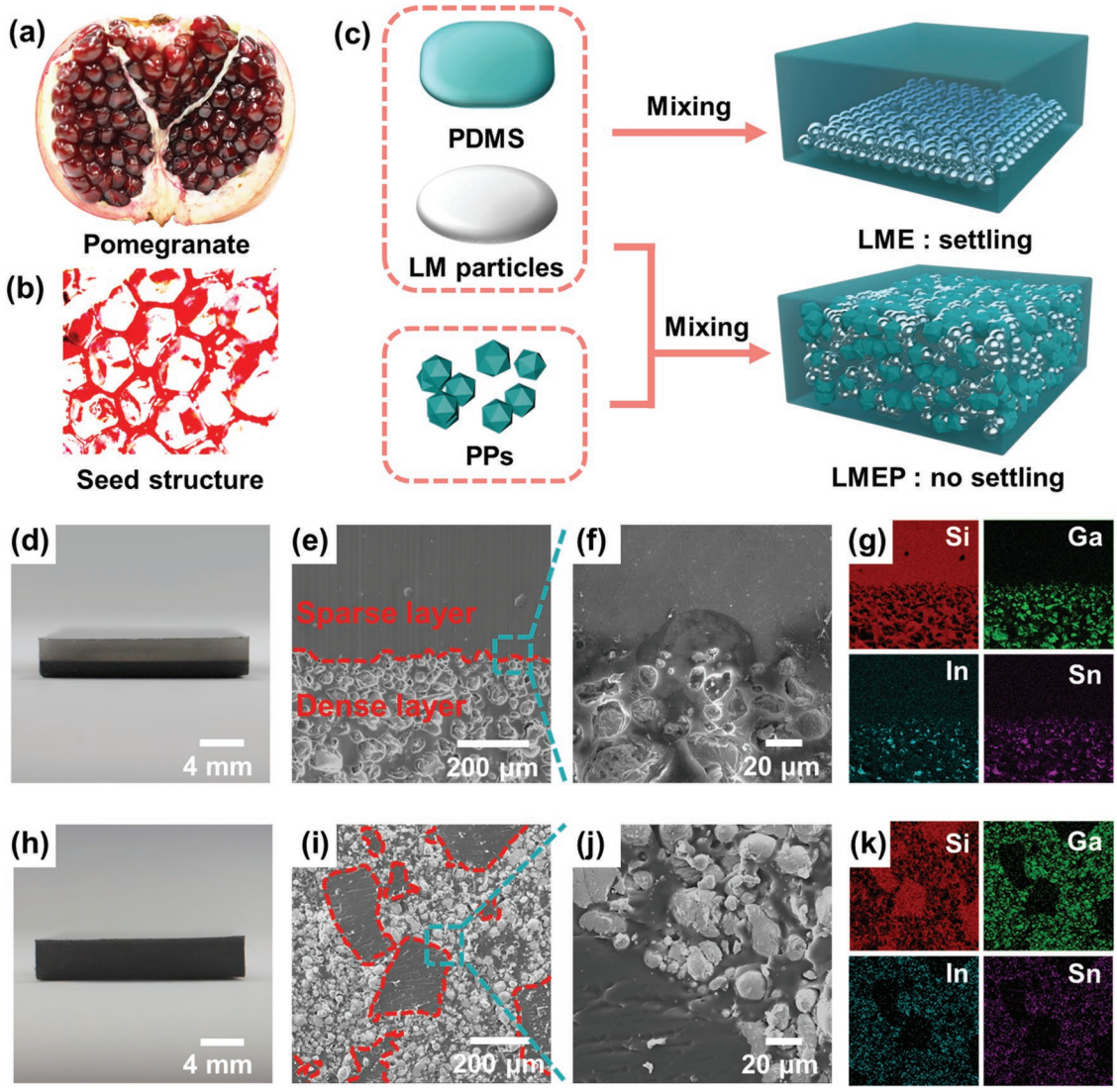

Figure 1. Characterization of the liquid metal elastomer with particles (LMEP). a) Photo of pomegranate seeds as a biological inspiration in which the seeds are similar to the PPs and the interstitial spaces are where LME resides. b) The structure of pomegranate shows seeds with interstitial spaces. c) Schematic of the fabrication processes of the settled LME and LMEP. d) Photo of the settled LME (ϕ_{LM} = 20%) due to settling of LM particles. e,f) SEM images of the settled region of LME which leads to layers with sparse and dense concentrations of LM particles. g) EDS element mappings of the settled LME. h) Photograph of LMEP (ϕ_{LM} = 20%, ϕ_{PPs} = 20%). i,j) SEM images of the LMEP. k) EDS element mappings of LMEP.

thermal pathways, and increases the volume fraction of conductive materials in the LME. However, the addition of such rigid additives can have a deleterious effect on the mechanical properties.[3a,17] For this reason, we explored soft elastomeric fillers.

To minimize settling, we take inspiration from pomegranate seeds. These seeds are particles that achieve uniform dispersion in space through jamming, as shown in **Figure 1**a,b. In this paper, we demonstrate an LME with polydimethylsiloxane particles (LMEP). Introducing polydimethylsiloxane particles (PPs) generates a jamming effect inside LMEP prior to curing, avoiding the settlement of LM particles and solving the problem of decreased dielectric constant, electrical and thermal conductivity without deteriorating the mechanical properties. Meanwhile, compared to LMEs with the same electrical conductivity, LMEPs lower the amount of LM needed to achieve conductive paths. The presence of the PP filler creates interstitial space occupied by the liquid metal particles. Interestingly, we discovered that the LMEP is inherently conductive without any additional mechanical sintering step, yet it can be rendered insulating by stretching beyond 100% strain; this suggests the particles are in gentle contact at rest, but not fully merged as evident by the ability to pull them apart with strain. This result is unexpected since normally LME must be mechanically sintered (i.e., physically pressed) to merge the particles together in a way that is not reversible.

Herein, we analyze the mechanism of the jamming effect and investigate the dielectric constant, electrical and thermal conductivity of LMEPs by changing the volume fractions of LM, polydimethylsiloxane (PDMS) pre-polymer (we call this

pre-polymer "PDMS" to distinguish it from the PPs), and PPs. We fabricate soft sensors of stress and tensile forces based on LMEPs with the optimal ratio, and present potential applications in the field of wearable electronics. In addition, we use uncured LMEPs as conductive ink to fabricate soft circuits on different substrates.

2. Results and Discussion

2.1. Mechanism of LMEP

Figure 1c shows the preparation processes of the LMEP and a control sample of conventional LME. For the LME, bulk LM, and PDMS were mixed by shear force, producing LM particles with a diameter from 10 to 100 µm. In ambient conditions, LM particles settle due to gravity, resulting in a "layered" LME consisting of a particle rich region (bottom) and silicone rich region (top). Notably, settlement of LM particles begins to occur immediately, gets worse with time, and is difficult to completely avoid. In other words, immediately solidifying the uncured LME at elevated temperatures can make LME in which layering is not visually apparent, although there is likely still some settling. As shown in Figure S1 (Supporting Information), with the same LM volume fraction, the cured LME at room temperature (settled LME) had more apparent layering than the cured LME at elevated temperatures.

To give a sense of time scales, we provide a brief scaling analysis of the forces involved with settling. Assuming LM particles as approximately spherical, the LM particles inside LME are subjected to gravity, buoyancy, and drag force (the latter occurs only if the particles are moving). The gravity of LM particles is seven times larger than that of PDMS, which leads to the settlement of LM particles. The drag force (F_d) on LM particles in the viscous PDMS medium can be expressed by the Stokes formula:

$$F_d = 6\pi\mu R v \tag{1}$$

μ represents the viscosity of the PDMS, R is the radius of the LM particles, v is the velocity of the LM particles relative to the PDMS. In particular, the drag force of an LM droplet is mainly due to the viscosity of the PDMS solution. Equation 2 balances the steady state forces of gravity, buoyancy, and drag on the LM particles in PDMS,

$$\frac{4\pi R^3}{3}\rho_{LM}g - 6\pi\mu R v - \frac{4\pi R^3}{3}\rho_{PDMS}g = 0 \tag{2}$$

in which ρ_{LM} and ρ_{PDMS} represent the density of the LM and PDMS, respectively. According to the Stokes' flow settling, the velocity of LM particles inside PDMS can be approximated expressed as:

$$v = \frac{2\left(\rho_{LM} - \rho_{PDMS}\right)}{9\mu} R^2 g \tag{3}$$

Based on the above analysis, reducing the radius of the LM particles or increasing the viscosity of the PDMS can suppress the settlement of the LM particles. This also explains the reason why the LM particles with smaller diameters (<1 µm) suspend in the upper region of the settled LME. We can calculate the steady-state velocity by plugging in representative values to Equation 3. When the viscosity of PDMS is 50 000 cP, the sedimentation velocities of the LM particles are $\approx 6.7 \times 10^{-3}$ µm s^{-1} with a diameter of 10 µm and $\approx 2.7 \times 10^{-2}$ µm s^{-1} with a diameter of 100 µm, which is consistent with the calculated result of Michele et al.'s work.[10b] The particles in the work here are 10 to 100 µm and thus we would expect them to fall 144 µm over the course of an hour (the normalized height of the sample is 1 mm).

To address this settling issue, we added PPs to LME prior to curing. PPs were prepared by grinding cured silicone (please see the details in the Experimental Section). Figure S2 (Supporting Information) presents the geometry and diameter distribution of PPs (<225 µm). Introducing PPs into the LME solution generates a jamming effect, which obtains the highly dispersed LMEP that does not settle.[18] The resulting composite is paste-like prior to curing and we observe no evidence of settling, which suggests that the particles jam. Interestingly, we observe this behavior at PP concentrations (≈20% by volume) well below percolation ,i.e., contact between PP particles. This suggests that the LM particles may also contribute to jamming. After curing, the resulting material is elastomeric.

To illustrate the concept, we prepared settled LMEs and LMEPs with volume fraction (ϕ) of LM = 20%. The settlement of the LM particles inside the LME is visible after settling at room temperature for 12 h, as shown in Figure 1d. The color of the LM rich layer is darker than that of the sparse layer due to the settlement of the large LM particles (10–100 µm in diameter).

Figure 1e,f shows the scanning electron microscope (SEM) images of the LME. LM particles are in the dense layer, as shown in Figure 1e. Figure S3a (Supporting Information) shows the particle diameter distribution of the LM particles (10–100 µm). Energy dispersive X-ray spectroscopy (EDS) map characterization further reveals the distribution of the LM particles.

Introducing PPs to the LME solution prevents the LM particles from settling, as shown in Figure 1h,i. Figure S3b (Supporting Information) shows the LM particle size distribution of the LMEP (ϕ_{LM} = 20%, ϕ_{PPs} = 20%). The LM particle diameters of the LMEP (ϕ_{LM} = 20%, ϕ_{PPs} = 20%) are ≈10 µm, which is smaller than that of LME. This phenomenon can be explained by adding PPs increases the viscosity of LMEP solution, generating LM particles with smaller diameters.[11c] In Figure 1j, there are no cracks or defects at the interfaces of PPs and PDMS, verifying good interfacial adhesion. The EDS mapping results also prove that the LM and PDMS are well dispersed. In addition, we photographed the topography of the LMEP at 110× magnification, as shown in Figure S4 (Supporting Information).

We used a camera to record the curing process of LME and LMEP with ϕ_{LM} = 30%, as shown in Figure S5 (Supporting Information). In Figure S5a, b (Supporting Information), as time increases, the LM particles in the LME and LMEP (ϕ_{LM} = 30%, ϕ_{PPs} = 10%) settled before curing at room temperature. While, increasing ϕ_{PPs} from 10% to 20% induces a jamming effect, which leads to a uniform LM particle distribution. As

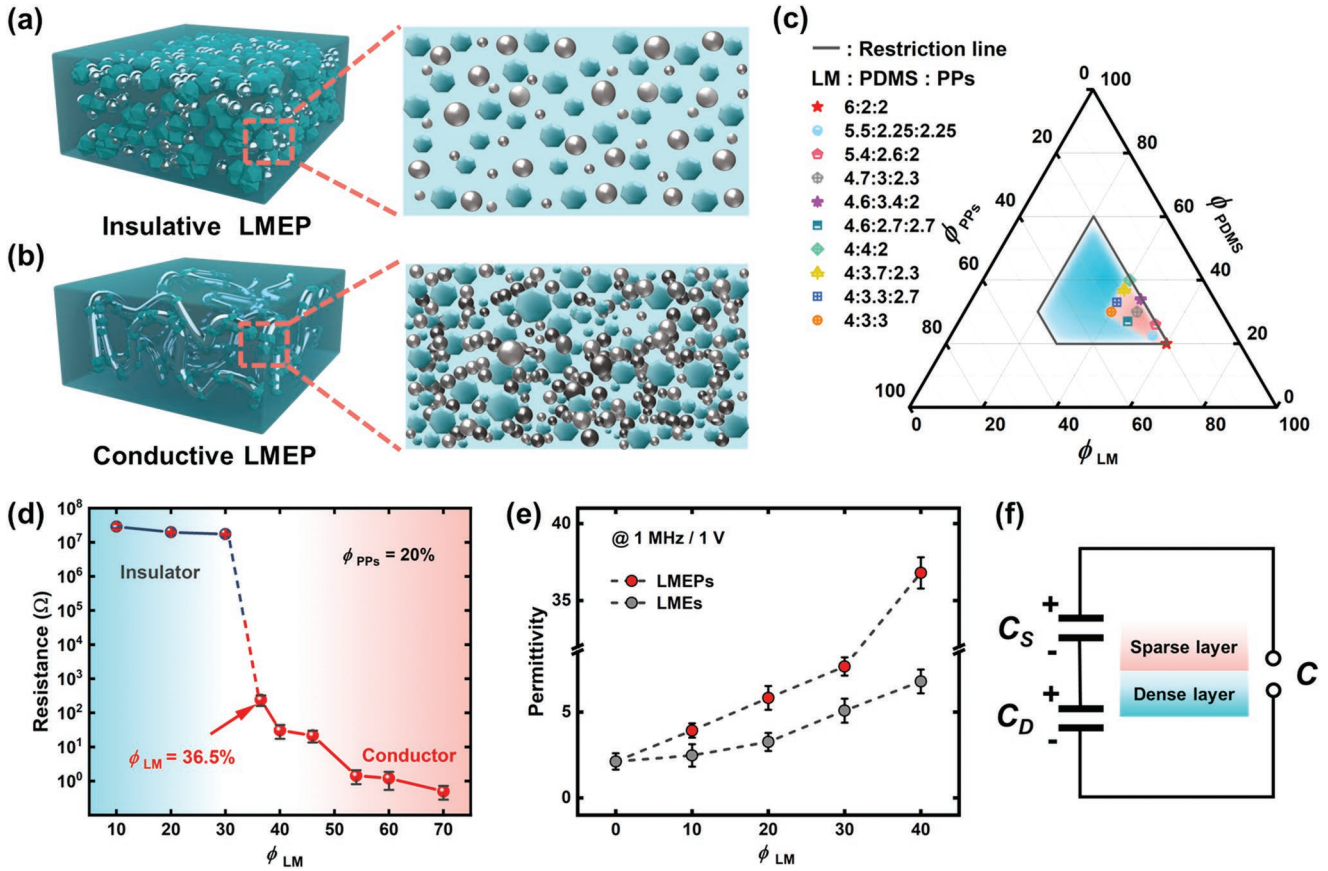

Figure 2. Conductive and dielectric characterization of the LMEP. Schematics of a) insulative LMEP and b) conductive LMEP. c) Ternary phase diagram of LMEP. We studied compositions within the "restriction line". d) Conductive threshold of the LMEP with ϕ_{PPs} = 20%. e) Plot of dielectric constant versus ϕ_{LM} of the settled LMEs and the LMEPs. f) Capacitance schematic of a settled LME.

shown in Figure S5b–d (Supporting Information), as ϕ_{PPs} increases, the delamination interface of the samples rises. Samples in Figure S5a,b (Supporting Information) show visible sedimentation. However, LMEP with ϕ_{PPs} above 20% did not settle, which indicates that ϕ_{PPs} = 20% is sufficient to avoid sedimentation. We repeated the LMEP experiment without any curing agent in the silicone. In the absence of a curing agent, the silicone remains in the liquid state. Even without the curing agent, the LM remained suspended over the duration of the 48 h experiment, suggesting the LMEP structure is truly stable. The above analysis shows that introducing PPs solves the layered problem of LME.

2.2. Electrical Properties of LMEP

To investigate the effect of PPs on the electrical properties of LMEPs, we analyzed and prepared LMEPs with different ϕ_{LM}, ϕ_{PPs}, and ϕ_{PDMS}. As shown conceptually in **Figure 2**a,b, adding a small amount of LM (10%< ϕ_{LM} < 30%) does not form conductive paths. However, the LMEP with ϕ_{LM} = 40% is conductive, indicating the volume fraction of LM particles determines the electrical properties of the LMEP. Note that the overall ϕ_{LM} is 40% in the LMEP, but in the interstitial spaces ϕ_{LM} = 50% (in other words, the PPs have no liquid metal and therefore their presence lowers the overall concentration of LM in the LMEP). Notably, the LMEP with ϕ_{LM} = 40% is conductive without any intentional sintering, which is surprising considering LME usually requires mechanical sintering to achieve conductivity due to the need to rupture thin layers of silicone between the LM particles. We will discuss this observation later in this section.

To systematically investigate the electrical conductivity, we construct a ternary phase diagram of LM particles, PDMS, and PPs, as shown in Figure 2c. The pink and blue areas are the parameter ranges of conductivity and non-conductivity, respectively. We created samples within the restriction line with ϕ_{LM} from 40% to 70%, ϕ_{PDMS} from 20% to 60%, and ϕ_{PPs} from 20% to 50%. These parameter ranges are based on three reasons: 1) the LMEP with ϕ_{PDMS} > 70% is non-conductive regardless of LM loading in the interstitial space. 2) According to prior work,[19] the maximum ϕ_{LM} in an LME is ≈81.8%. Further increasing ϕ_{LM} induces LM to exude from the LME. 3) The uncured LMEPs with ϕ_{PPs} > 50% are highly viscous, which hinders the processability, as shown in Figure S6 (Supporting Information). Meanwhile, we impose two volume fraction constraints: $\phi_{PDMS} \geq \phi_{PPs}$ and $\phi_{LM} \geq \phi_{PPs}$. Based on the above constraints, we identified regions of conductive LMEPs, as shown in Figure 2c.

The conductivity of the LMEP reported in Figure 2 is surprising considering LMEs with similar compositions are not electrically conductive until they are deliberately pressed (or

peeled from a surface) to render them conductive. This process has been referred to as "mechanical sintering" in the literature. Such mechanical forces are presumed to rupture the thin layers of elastomer that form between particles and thereby create conductive pathways through the LME. Here, we measured the conductivity without applying any mechanical forces (or peeling) after curing the LMEP. Thus, the observation of conductivity without sintering is surprising.

There are several studies that report conductive LMEs without deliberately applying external mechanical forces to percolate the particles. One study reports conductivity by cooling the LME to very low temperatures.[20] Low temperatures have two effects: 1) they can freeze the metal, thereby causing it to expand and improving the chances of forming particle-particle contact, and 2) they can vitrify the polymer so it stiffens, which is important for creating percolation. In prior studies, warming the LME reverts the material back to an insulating state, suggesting that particles are no longer in contact.[10c,20] Yet, the LMEP reported herein remains conductive at room temperature and does not need thermal cycling.

To avoid the influence of unintentional mechanical sintering, we compared the conductivity of uncured LMEP (ϕ_{LM} = 40%, ϕ_{PPs} = 30%) (without removing it from the mixer) and uncured LME (ϕ_{LM} = 40%) using the two-point probe method, as shown in Video S1 (Supporting Information). We made the measurements immediately after mixing to avoid hysteretic effects from settling in the LME control. The conductivity of the LMEP with ϕ_{LM} = 40% is intermittent (recall, 40% is at the percolation threshold). However, the uncured LME with ϕ_{LM} = 40% is non-conductive (a resistance that exceeds the limit of the multimeter).

There are two factors that may explain this surprising observation of conductivity without sintering. First, the effective LM concentration (50%) in the interstitial spaces between PPs is higher than the overall concentration (40%). Yet, this cannot alone explain the conductivity because LMEs at 50% loading of LM only become conductive after mechanical sintering. After transferring (scraping) the uncured yet paste-like LMEP and the uncured LME into molds, we measured the conductivity of the uncured LMEP and the uncured LME using the two-probe method, as shown in Video S2 (Supporting Information). In the video, the uncured LMEP was conductive while the uncured LME was not. This observation implies that handling the LMEP may push the LM particles closer together due to its paste-like consistency prior to curing. Thus, we reason that the forces from "smearing" the LMEP into a mold prior to curing sinters some of the particles. We took a cross-sectional electron micrograph of the LMEP (ϕ_{LM} = 40%, ϕ_{PPs} = 30%), as shown in Figure S4b (Supporting Information). To avoid merging LM particles during the sample cutting, we used liquid nitrogen to transform LM particles into solid particles. The outlines of the LM particles were clear, indicating that LM particles are not fully sintered. Second, based on the above observations and analyses, the uncured LMEP with intermittent conductivity can be explained by the mixing process applying shear stress to the uncured LMEP, which makes PPs squeeze LM particles. Due to the high effective volume fraction, the squeezing of PPs sinters small amounts of LM particles, leading to intermittent conductivity (not stable conductive paths).

Based on the above results, we measured the conductivity of virgin LMEPs and each sample was measured six times, as shown in Figure S7 (Supporting Information). We prepared LMEPs with length, width, and height of 20, 20, and 4 mm, respectively, and placed copper foils on the top of the sample at each end based on a gravity direction. To reduce the contact resistance of the measurement, the samples were connected to the copper foil with conductive silver paste.[21] The conductivities are in the range of 0—450 S m^{-1}. The LMEP with ϕ_{LM} = 60%, ϕ_{PPs} = 20% has the highest conductivity of 438 S m^{-1}. These measurements were done without peeling the samples from the substrate, which is important since peeling can inadvertently cause sintering.[22] For comparison, we measured the conductivity of the LMEP (ϕ_{LM} = 60% and ϕ_{PPs} = 20%) after mechanical sintering (30% compressive strain). The conductivity of the sintered sample reaches 2170 S m^{-1} in Figure S8a (Supporting Information), which presents the same phenomenon as the observation of Carmel Majidi's group.[7] For a given ϕ_{PPs}, the conductivity of the LMEP increases with higher ϕ_{LM}, as expected. The conductivity of LMEPs with the same ϕ_{LM} increases with the increase of ϕ_{PPs}, indicating the jamming results in better conductive paths. LME samples prepared in the same way and with identical loading of LM had conductivity values of 1×10^{-6}S m^{-1}.

Figure 2d presents the plot of the resistance of the virgin LMEPs versus ϕ_{LM}. Each sample in Figure 2d was measured six times. We used ϕ_{PPs} = 20% in these studies because that proved sufficient to prevent settling. When the ϕ_{LM} is <30%, the resistance of the LMEP decreases gradually with the increase of ϕ_{LM}. The resistance of the LMEP decreases ten orders of magnitude when ϕ_{LM} > 36.5%. The resistance of the LMEP tends to decrease gradually with increase in ϕ_{LM} > 50%. The threshold of LMEP is lower than that of LME, which reduces the cost and density. Due to the same cost and density of the PPs and the PDMS, with the same geometry (20 mm × 20 mm × 4 mm in length, width, and height), LMEP is 0.61 dollar mL^{-1} cheaper than LME and 0.78 g mL^{-1} lighter. Notably, LMEPs with ϕ_{LM} = 36.5%, ϕ_{PPs} = 20% are naturally conductive. On the contrary, prior studies of LMEs with ϕ_{LM} < 40%, which were cured rapidly to avoid settling—must be mechanically sintered to realize electrical conductivity, as shown in Table S1 (Supporting Information). To confirm, we prepared control samples by using the exact same materials and processes of LMEP while excluding the PPs (ϕ_{LM} = 40%) which is insulative without sintering.

According to the findings of Figure 2d, when LM volume fraction is below a certain value (≈36.5%), LMEPs are not conductive, so we can consider them as dielectrics. Figure 2e presents the plot of the dielectric constants of settled LMEs and LMEPs (ϕ_{PPs} = 30%) versus ϕ_{LM}. The dielectric constants of settled LMEs and LMEPs increase with the increase of ϕ_{LM}, as expected.[3a,9a] The dielectric constants of the LMEP are higher than that of the settled LME because the jamming effect keeps the LM particles well-dispersed. When ϕ_{LM} increases from 30% to 40%, the effective dielectric constant of the LMEP changes from 7.7 to 36.7, indicating the formation of conductive paths. These paths are equipotential within the LMEP, thereby increasing the effective dielectric properties.[9a] To further investigate the dielectric properties of the LMEP.[17] Figure S9a (Supporting Information) shows the dielectric loss of settled LMEs

and LMEPs (ϕ_{PPs} = 30%) versus ϕ_{LM}. LMEPs exhibit lower dissipation factors (0.02), although they increase with the ϕ_{LM}. Figure S9b (Supporting Information) displays the breakdown strength of LMEs and LMEPs(ϕ_{PPs} = 30%) with different ϕ_{LM}. The breakdown strength of LMEP is lower than that of LME due to the highly dispersed LM particles, forming a breakdown circuit at a lower voltage. And when ϕ_{LM} = 30%, the breakdown strength drops sharply (LME from 21.5 to 8.83 kV mm^{-1}, LMEP from 17.16 to 8.42 kV mm^{-1}) due to the percolation. Figure S10 (Supporting Information) investigates the dielectric properties of the samples at different frequencies. The dielectric constant of all the samples shows a decreasing trend with increasing frequency, which is consistent with previous work.[23] The above measurements are based on virgin samples. Each sample was measured ten times.

Figure 2f explains the reason why the dielectric constant of the LMEP is larger than that of the settled LME. The LM particles distribute in the dense and sparse layers of the settled LME. Assuming the capacitance of the sparse and dense layers are C_S and C_D, respectively. The capacitance (C) of the settled LME can be considered as the series connection of two capacitors:

$$C = \frac{1}{\frac{1}{C_s} + \frac{1}{C_D}} \tag{4}$$

C is the largest when $C_S = C_D$. In other words, highly dispersed LM particles bring in the highest dielectric constant, which indicates the introduction of PPs in LMEPs guarantees the high dielectric constant.

2.3. LMEP-Based Capacitive Stress Sensor

As a demonstration of the utility of LMEP, we created a stress sensor. LMEP with ϕ_{PPs} = 30% sandwiched by two electrodes composed of the LMEP-based capacitive stress sensor. **Figure 3**a shows photos and schematics of the LMEP-based capacitive stress sensor before and after compression. Benefitting from the LMEP with a high dielectric constant, the LMEP-based capacitive stress sensor has a high sensitivity. We prepared LMEPs and non-settled LMEs with ϕ_{LM} = 0%, 10%, and 30%. The capacitance of virgin LMEs and virgin LMEPs as shown in Figure S11 (Supporting Information). Figure 3b shows the stress–strain curves of virgin non-settled LMEs and virgin LMEPs. Increasing ϕ_{LM} increases the slope of the stress–strain curves. The loading and unloading curves can return to the initial point without plastic deformation. In addition, we measured the strain-stress curves of a virgin LME (ϕ_{LM} = 30%) and a virgin LMEP (ϕ_{LM} = 30%, ϕ_{PPs} = 30%). In Figure S12a,d (Supporting Information), after applying 30% compressive strain, the virgin LME (ϕ_{LM} = 30%) presents plastic deformation (≈ 0.4%). While, in Figure S12c,d (Supporting Information), the plastic deformation of LMEP (ϕ_{LM} = 30%, ϕ_{PPs} = 30%) is negligible after the first cycle, showing a better mechanical property. Meanwhile, the presence of PPs deteriorates the hysteresis due to the increase in the internal friction. Figure S12e–h (Supporting Information) depicts the strain–stress curves of LME (ϕ_{LM} = 10%), LMEP (ϕ_{LM} = 10%, ϕ_{PPs} = 30%), LME (ϕ_{LM} = 30%), and LMEP (ϕ_{LM} = 30%, ϕ_{PPs} = 30%) from 10% to 30% compressive strain, which exhibit the Mullins effect. Figure S13 (Supporting Information) depicts

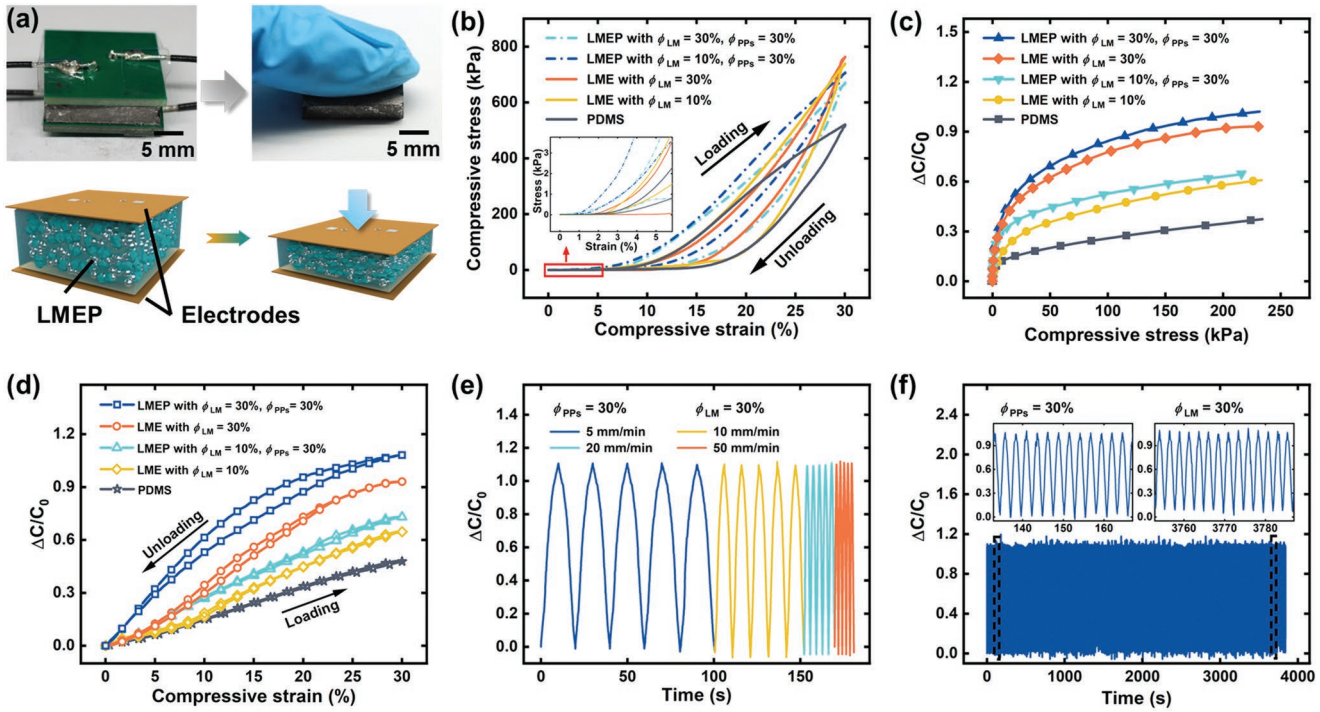

Figure 3. Characterization of the LMEP-based capacitive stress sensor. a) Photos and schematics of the sensor before and after compression. b) Mechanical properties of LMEP. c) Plot of $\Delta C/C_0$ versus compressive stress for LMEs and LMEPs. d) Plot of $\Delta C/C_0$ comparison of LMEPs compressed to 30% strain. e) Frequency-independent response of the LMEP. f) Durability test of LMEP over 1500 compression cycles.

the virgin LMEP (ϕ_{LM} = 40%, ϕ_{PPs} = 30%) under 20% to 60% tensile strain. The sample also exhibits the Mullins effect, which changes stress–strain curves. Before data collection in Figure 3c–f, the samples have gone through the break-in period (30% compressive strain for ten cycles). Figure 3c shows the plot of stress versus capacitance variation ratio ($\Delta C/C_0$). The $\Delta C/C_0$ increases with higher ϕ_{LM}. LMEP exhibits a higher capacitance variation ratio than LME with the same ϕ_{LM}. The highest $\Delta C/C_0$ reaches 0.993 (LMEP with ϕ_{LM} = 30%, ϕ_{PPs} = 30%). In Figure 3d, the hysteresis of the LMEP-based sensor is larger than that of the LME-based sensor, which may be attributed to friction and stress concentration between the PPs, PDMS, and LM particles. Hysteresis is the degree of inconsistency between the loading and unloading curves, it is usually expressed as the percentage of the maximum difference between the two curves and the full scale output representing the viscoelasticity.[9b,24] We calculated the degree of hysteresis (DH) to express the hysteresis phenomenon of the LMEP:

$$DH = \frac{A_L - A_U}{A_L} \times 100\% \quad (5)$$

where A_L and A_U are the area of loading and unloading curves, respectively. A smaller DH value would mean lesser hysteresis of electrical signal response. The LMEP-based sensor (ϕ_{LM} = 30%, ϕ_{PPs} = 30%) has a hysteresis of 7.82%, giving a cushion that protects the objects it touches. The $\Delta C/C_0$ of the LMEP-based sensor (ϕ_{LM} = 30%, ϕ_{PPs} = 30%) under different stress rates are shown in Figure 3e. The $\Delta C/C_0$ shows stability even if the stress rate is increased by a factor of 10 (from 5 to 50 mm min^{-1}). The $\Delta C/C_0$ cycling curve of the LMEP-based sensor (ϕ_{LM} = 30%, ϕ_{PPs} = 30%) is shown in Figure 3f. The sensor has no structural damage and no $\Delta C/C_0$ drift over 1500 cycles under 600 kPa.

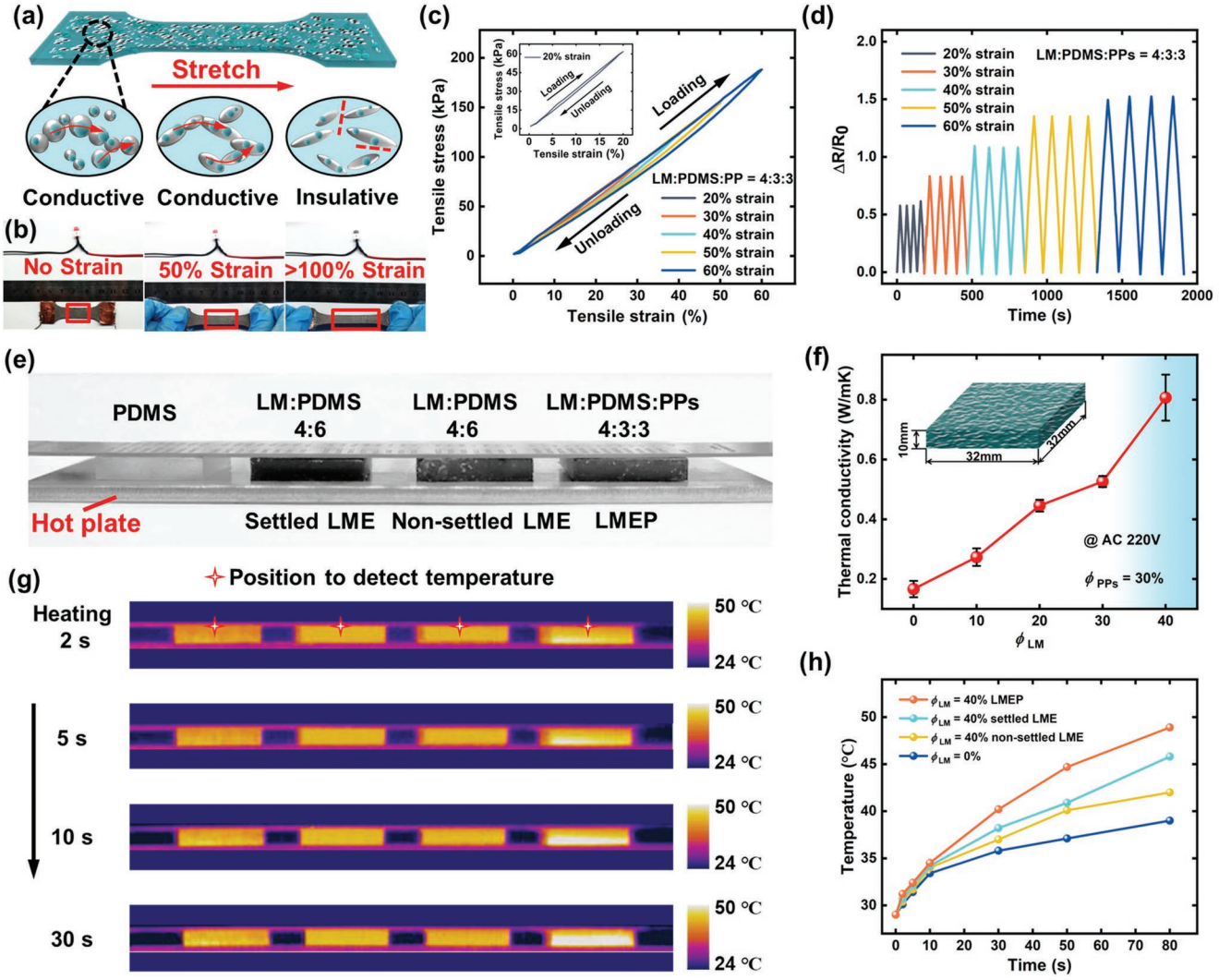

Figure 4. Characterization of LMEP-based resistive tensile sensor and thermal properties. a) Schematics of LMEP-based resistive sensor during stretching. b) Stretching the sensor in series with LED. c) Mechanical stretching properties of LMEP. d) Cyclic tensile tests of a sensor from 20% to 60% strain. e) Photo of the thermal conductivity experiment. f) Plot of thermal conductivities versus ϕ_{LM}. g) Infrared thermal images of PDMS, settled LME, non-settled LME, and LMEP with heating time. h) Plot of marked point temperature versus heating time.

2.4. LMEP-Based Resistive Tensile Sensor

The conductivity of the LMEP at $\phi_{LM} > 30\%$ enables the application of resistive tensile sensors. We fabricated resistive tensile sensors based on the LMEP with $\phi_{LM} = 40\%$, $\phi_{PPs} = 30\%$, and $\phi_{PDMS} = 30\%$. The LMEP-tensile sensor is 60 mm × 20 mm × 1 mm in length, width, and height. **Figure 4**a shows the schematic of the LMEP-based resistive tensile sensor. In the initial state, LM particles form conductive paths in the LMEP. Stretching the sensor deforms the LM particles conductive paths, which narrows or even breaks the conductive paths. In Figure 4b, the sensor was connected to a light-emitting diode (LED) bulb. As the tensile strain increases, the LED becomes dimmer and the circuit resistance increases. When the strain was >100%, the LED turned off, and the LM conductive paths were disconnected. This is an important observation because it suggests that the particles never truly sintered; that is, they did not form a continuous liquid path. Instead, it appears that they are just in close proximity and sufficiently high strain can pull them apart to render the sample insulating.

Figure 4c shows the stress–strain curves at different strains (20–60%). In this experiment, the sensor has undergone a tensile break-in period (ten cycles). The unloading curves can restore to the initial point without plastic deformation, demonstrating good stretchability. Figure S13 (Supporting Information) depicts the virgin LMEP ($\phi_{LM} = 40\%$, $\phi_{PPs} = 30\%$) under 20% to 60% tensile strain. The sample also exhibits the Mullins effect, which changes stress–strain curves. Before the experiment in Figures S14 and S4d (Supporting Information), we have used this sample to measure mechanical property, which sinters some LM particles and increases the conductivity of the LMEP. Figure S14a (Supporting Information) plots the strain–resistance curves of the sensor. In Figure S14a (Supporting Information), applying tensile strain (from 20% to 60%) increases the resistance of the LMEP-based sensor from 0.23 to 0.57 Ω, having a sensitivity of 8.4×10^{-2} kPa^{-1}. According to the calculation equation of sensitivity (Equation 6):

$$S = \frac{\delta(\Delta R/R_0)}{\delta P} \tag{6}$$

lower initial resistance significantly improves sensitivity,[7] leading to a decent piezoresistivity. The stress-resistance curves at strains from 20% to 60% are shown in Figure S14b (Supporting Information). In Figure 4d, the repeated test of the sensor under tensile strains (20–60%) shows good stability.

2.5. Thermal Conductivity of LMEP

LMEPs also have excellent thermal conductivity. Figure 4f shows the thermal conductivity of LMEPs with ϕ_{LM} from 0 to 40% (32 mm × 32 mm × 10 mm). The increase in thermal conductivity of LEMP is not linearly related to the increase of ϕ_{LM}. As $\phi_{LM} < 30\%$, there is little percolation between LM particles. LMEPs with $\phi_{LM} < 30\%$ have continuous LM paths which promote electron and photon transport, reduce the interfacial thermal resistance, and form thermal conductive paths. The LMEP with $\phi_{LM} = 40\%$, $\phi_{PPs} = 30\%$, and $\phi_{PDMS} = 30\%$ has the highest thermal conductivity of 0.8 W m K^{-1}. Notably, air bubbles trapped in the LMEPs reduce the thermal conductivity. Without degassing, the air bubbles in LMEP ($\phi_{LM} = 30\%$, $\phi_{PPs} = 30\%$) are visible, as shown in Figure S15a (Supporting Information). Adequate degassing during preparation is needed to get desired thermal conductivity. The LMEP without air bubbles is shown in Figure S15b (Supporting Information). The density of the sample with bubbles is 2.531 ± 0.134 g mL^{-1}, and the density of the sample without bubbles is 2.928 ± 0.074 g mL^{-1}.

To further demonstrate the high thermal conductivity of LMEP, we placed a PDMS slab, settled LME with $\phi_{LM} = 40\%$, non-settled LME with $\phi_{LM} = 40\%$, LMEP with $\phi_{LM} = 40\%$, $\phi_{PPs} = 30\%$ on a heat plate (50 °C) to compare the thermal conductivities. A stainless steel plate above the sample was used as a heat sink, as shown in Figure 4e. The temperature gradients of the above four samples were identified using an infrared thermal imager, as shown in Figure 4g. Heat propagates faster in the sample of LM homogeneous dispersion, demonstrating the superior heat transport capability of LMEP. The thermal conductivity of the non-settled LME is worse than that of the LMEP. In Figure 4h, we compared the temperatures of the marked points in Figure 4g. The temperature of LMEP is the highest, indicating that the introduction of PPs highly disperses the LM particles and improves the electron and the photon transmission rate. In addition, we measured the specific heat capacity of the LMEPs ($\phi_{PPs} = 30\%$), LMEs with settling and LMEs without settling, as shown in Figure S16b (Supporting Information). With the increase in ϕ_{LM}, the specific heat capacity decreases, which is consistent with the observations of Jeong et al.[25]

2.6. Applications of LMEP

LEMP-based soft sensors can be used to monitor human motion. We attached the sensors to the finger, wrist, elbow, and knee joints as shown in **Figure 5**a–d. The sensor has the advantages of high sensitivity, high stretchability, and has potential applications in the fields of wearable electronics and human-machine interfaces.

In **Figure 6**a, a mold with a thickness of 1 mm and a width of 2 mm was made by laser engraving. We filled the uncured LMEP ink ($\phi_{LM} = 40\%$, $\phi_{PPs} = 30\%$) into the designed mold by handwriting and scraping. After curing, we got LMEP-based circuits, as shown in Figure 6c. LED bulbs can be connected to the circuits by using the uncured LMEP ink as a glue, generating soft LED circuits, as shown in Figure 6b–d. These circuits are soft, and can be repeatedly bent, twisted, and stretched without affecting the functionality. Notably, even at the 60% tensile strain, the resistance of the LMEP is only 0.57 Ω, which is reasonable for stretched circuit as shown in Figure S14a (Supporting Information). We use the uncured LMEP as conductive ink to fabricate soft circuits. We fabricated this circuit based on different substrates (PDMS, Teflon board, Teflon tape, and Ecoflex), as shown in Figure 6b–e. To investigate the width, we fabricated the traces with the width of 1.5, 1, and 0.5 mm, as shown in Figure S17 (Supporting Information). In addition, we found that the width of traces lower than 0.5 mm leads to an unstable electrical connection, which is limited by the diameter of PPs (≈225 µm). The uncured LMEP ink shows good adhesion on different substrates, indicating various applications.

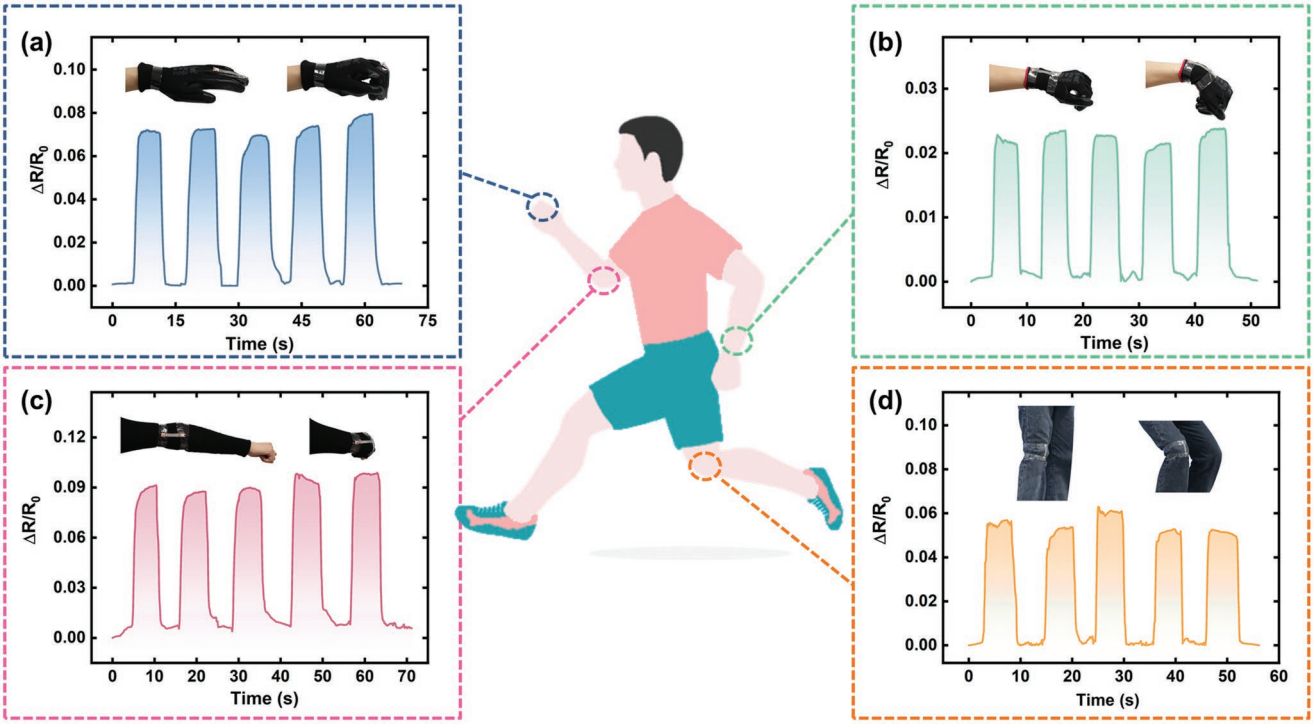

Figure 5. Human body motion measurement of LMEP-based resistive sensors at a) finger, b) wrist, c) elbow, and d) knee.

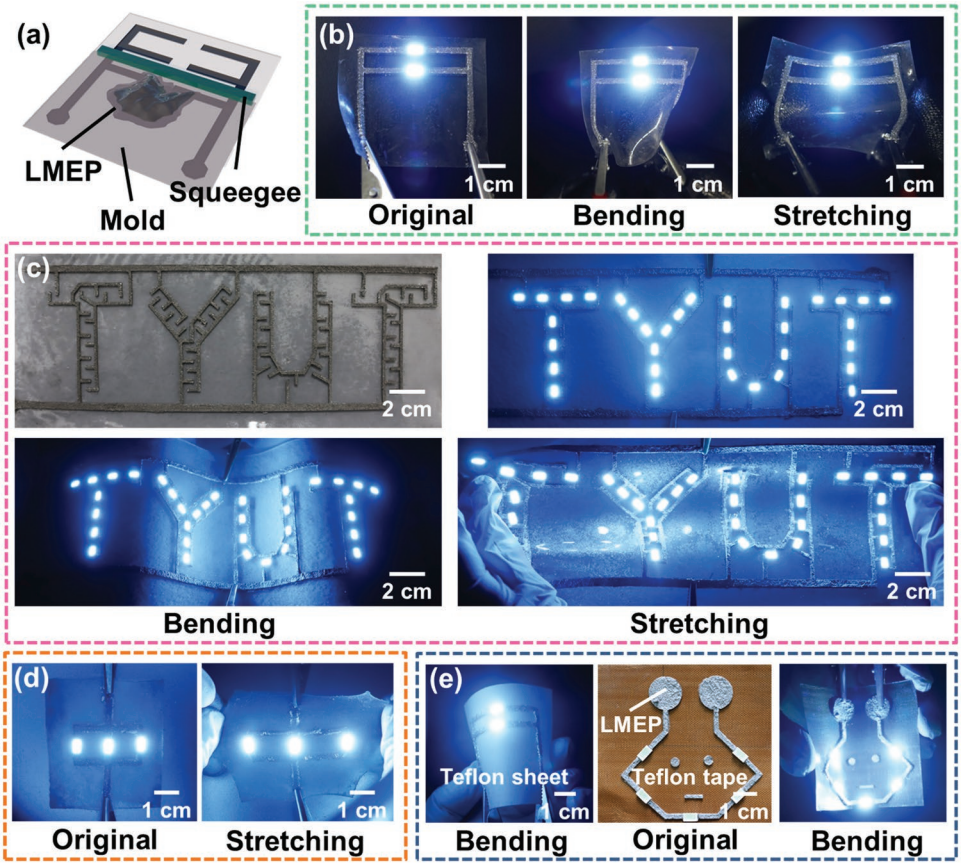

Figure 6. LMEP conductive ink. a) Schematic of stencil printing the LMEP ink. b,c) Photos of LMEP-based soft circuit. d) Stretchability of the LMEP-based soft circuit. e) LMEP-based soft circuit on Teflon sheet and tape.

3. Conclusion

In this work, inspired by pomegranate seeds, we fabricated LMEP by introducing PPs that generate the jamming effect. We investigated the mechanism of the jamming effect inside the LMEP, demonstrating the uniform dispersion of LM particles. Furthermore, by changing ϕ_{LM}, ϕ_{PPs}, we improved the dielectric constant, electrical, thermal conductivity, and reduced the cost and density. We fabricated stress and tensile sensors based on LMEP, tested their mechanical and electrical properties. The applications of the above sensors were also demonstrated. In additon, soft circuits were prepared by using the uncured LMEP ink, which has application potential in the fields of wearable electronics and human-machine interfaces.

4. Experimental Section

Materials: Galinstan was purchased from Shenyang Jiabei Trading Co., Ltd. PDMS (Sylgard 184) was purchased from Dow Corning. The molds were made by 3D printing. Electrodes were fabricated using a general printed circuit board fabrication process (20 mm × 20 mm × 0.2 mm). Acrylic slabs were supplied by Xinyi Acrylic Co., Ltd.

Fabrication Processes of LME and LMEP: PDMS elastomer base and curing agent were mixed in an 8:1 mass ratio by a vacuum mixer. The PDMS with a 10:1 mass ratio is too soft (2.64 ± 0.023 MPa) to be cut by the high-speed blade. However, PDMS with a mass ratio of 8:1 has a modulus of elasticity of 2.89 ± 0.067 MPa, which has a less mechanical effect on LM composites while increasing the hardness of PDMS. Then the PDMS was cured at 80 °C for 2 h. The prepared PDMS slab was cut by a grinder at 3000 rpm for 6 min. The PPs with a particle size of 100–225 µm were sieved with a 70 mesh.

PDMS elastomer base and curing agent were mixed in a 10:1 mass ratio by the vacuum mixer. Then the PDMS (i.e., pre-polymer) was mixed with bulk LM by the mixer for 2 min. LME was obtained by solidifying at 80 °C for 2 h. LME with settling was fabricated by curing the composites in ambient conditions for 12 h, resulting in particle settling.

The PPs and the LME suspension were mixed by hand for 2 min. Then the LMEP suspension was mixed by the mixer for 2 min. According to Figure S5 (Supporting Information), it was known that the LMEP didn't change after 48 h. So, the LMEP solution was cast at 80 °C for 2 h, the LMEP was fabricated.

The electrical characterization of LMEPs is using samples with 20 mm × 20 mm × 4 mm in length, width, and height. The LMEP-tensile sensor is 60 mm × 20 mm × 4 mm in length, width, and height. The conductivity measurements were done without peeling the samples from the substrate. The conductivity was measured by the two probe method. Two copper foils were placed on each end of samples based on gravity direction. A weight (9.8 g) was placed on the top electrode to ensure a stable connection.

Experimental Equipment: The PDMS slab was cut by a grinder (FW100, Shanghai Bensen Co., Ltd.) and sieved with a mesh (70, Screen Mesh Co., Ltd). PDMS and LMEs, and LMEPs were mixed by a vacuum mixer (HMV600, Shenzhen Hasai Technology Co., Ltd.). The optical images were captured using a Canon camera and a stereomicroscope (SZ680, Chongqing Aote Optical Instrument Co., Ltd). SEM images and EDS mapping images of LME and LMEP were taken with the TESCAN LYRA 3. SEM samples preparation: 1) Virgin LMEs and LMEPs were immersed into liquid nitrogen for 3 min. Then slicing the samples with a knife. 2) Spraying gold on samples by a lon sputtering instrument (108auto, Cressington Scientific Instruments Co.,Ltd) for 60 s. 3) After pasting the sample with conductive adhesives, the microstructure of samples was observed under 20 kV. SEM samples were virgin. The thermal conductivity of LMEPs and LMEs was measured by using a Hot Disk (TPS, HCDR-S, Nanjing Huicheng Instrument Co., Ltd), as shown in Figure S16a (Supporting Information). LMEPs without air bubbles were fabricated by applying a vacuum for 2 h before the curing process. Based on the theory of the transient planar heat source technique (TPS), two identical samples (32 mm × 32 mm × 10 mm) were placed on either side of the planar probe. The operating voltage was 220 V. By recording the temperature and response time of the probe, the thermal conductivity was measured. Each sample was measured six times.

The temperature distribution was taken with an infrared thermal imager (D600, SATIR Trade UK Co., Ltd). The horizontal distance between samples and the imager equipment was 0.5 m. The breakdown strength of the samples was measured by using an electroporation apparatus (ECM830, BTX), where the number of pulsed square waves was ten, the pulse time was 90 µs.

In a nitrogen atmosphere (20 mL min^{-1}), the heat capacities of the settled LMEs, non-settle LMEs, and LMEPs were measured by a differential scanning calorimeter (DSC 204, NETZSCH). The samples were placed in a disposable aluminum crucible. The standard sample was a sapphire with a known specific heat capacity. The temperature range was 0–50 °C and the heating rate was 10 K min^{-1}. The specific heat capacity at 25 °C was calculated by using the Proteus analysis software of the samples. Every sample was measured three times.

The mechanical properties were measured using a universal Testing Machine (Instron 5544). The capacitance and the electric conductivity were measured by a LCR (HIOKI IM3536) and a source meter (Keithley 2450), respectively. The electrical resistance was measured by the two-point method. Samples were sandwiched by two copper foils. To ensure stable electrical contact, one weight (8.4 g) was placed on the top electrode.

All experiments complied with guidelines by the Taiyuan University of Technology. All subjects were volunteers (co-authors of the work) and provided informed consent (Project nr.: 62101432).

Supporting Information

Supporting Information is available from the Wiley Online Library or from the author.

Acknowledgements

The authors acknowledge support from the National Natural Science Foundation of China (grant no. 62101432), the Fundamental Research Program of Shanxi Province (grant no. 20210302123182), the Research Project of Shanxi Scholarship Council of China (grant no. 2020-036, 2022-069) and the Scientific Research Fund of Zhejiang Provincial Education Department (grant no. Y202146138).

Conflict of Interest

The authors declare no conflict of interest.

Data Availability Statement

Research data are not shared.

Keywords

eutectic gallium indium, soft circuits, tactile sensors, tensile sensors, thermal conductors

Received: September 10, 2022
Revised: November 10, 2022
Published online:

[1] a) M. D. Dickey, *Adv. Mater.* **2017**, *29*, 1606425; b) S.-Y. Tang, C. Tabor, K. Kalantar-Zadeh, M. D. Dickey, *Annu. Rev. Mater. Res.* **2021**, *51*, 381.

[2] a) N. Kazem, T. Hellebrekers, C. Majidi, *Adv. Mater.* **2017**, *29*, 1605985; b) S. Chen, H.-Z. Wang, R.-Q. Zhao, W. Rao, J. Liu, *Matter* **2020**, *2*, 1446; c) N. Kazem, M. D. Bartlett, C. Majidi, *Adv. Mater.* **2018**, *30*, 1706594.

[3] a) M. D. Bartlett, A. Fassler, N. Kazem, E. J. Markvicka, P. Mandal, C. Majidi, *Adv. Mater.* **2016**, *28*, 3726; b) A. Fassler, C. Majidi, *Adv. Mater.* **2015**, *27*, 1928; c) G. Yun, S. Y. Tang, S. Sun, D. Yuan, Q. Zhao, L. Deng, S. Yan, H. Du, M. D. Dickey, W. Li, *Nat. Commun.* **2019**, *10*, 1300.

[4] Y. M. Xin, H. Peng, J. Xu, J. Y. Zhang, *Adv. Funct. Mater.* **2019**, *29*, 1808989.

[5] a) Y. T. Hao, J. Y. Gao, Y. G. Lv, J. Liu, *Adv. Funct. Mater.* **2022**, 32; b) B. S. Chang, R. Tutika, J. Cutinho, S. Oyola-Reynoso, J. H. Chen, M. D. Bartlett, M. M. Thuo, *Mater. Horiz.* **2018**, *5*, 416.

[6] a) M. H. Malakooti, N. Kazem, J. J. Yan, C. F. Pan, E. J. Markvicka, K. Matyjaszewski, C. Majidi, *Adv. Funct. Mater.* **2019**, *29*, 1906098; b) M. Zadan, M. H. Malakooti, C. Majidi, *ACS Appl. Mater. Interfaces* **2020**, *12*, 17921; c) Y. Sargolzaeiaval, V. P. Ramesh, T. V. Neumann, V. Misra, D. Vashaee, M. D. Dickey, M. C. Ozturk, *Appl. Energy* **2020**, *262*, 114370.

[7] E. J. Markvicka, M. D. Bartlett, X. Huang, C. Majidi, *Nat. Mater.* **2018**, *17*, 618.

[8] a) Y. C. Lai, H. W. Lu, H. M. Wu, D. G. Zhang, J. Y. Yang, J. Ma, M. Shamsi, V. Vallem, M. D. Dickey, *Adv. Energy Mater.* **2021**, *11*, 2100411; b) M. J. Ford, D. K. Patel, C. Pan, S. Bergbreiter, C. Majidi, *Adv. Mater.* **2020**, *32*, 2002929; c) Y. Lin, C. Cooper, M. Wang, J. J. Adams, J. Genzer, M. D. Dickey, *Small* **2015**, *11*, 6397.

[9] a) J. Y. Yang, D. Tang, J. P. Ao, T. Ghosh, T. V. Neumann, D. G. Zhang, Y. Piskarev, T. T. Yu, V. K. Truong, K. Xie, Y. C. Lai, Y. Li, M. D. Dickey, *Adv. Funct. Mater.* **2020**, *30*, 2002611; b) J. Yang, K. Y. Kwon, S. Kanetkar, R. Xing, P. Nithyanandam, Y. Li, W. Jung, W. Gong, M. Tuman, Q. Shen, M. Wang, T. Ghosh, K. Chatterjee, X. Wang, D. Zhang, T. i. Kim, V. K. Truong, M. D. Dickey, *Adv. Mater. Technol.* **2021**, *7*, 2101074; c) D. G. Zhang, Y. Q. Zhong, Y. L. Wu, X. F. Zhang, M. D. Dickey, J. Y. Yang, *Compos. Sci. Technol.* **2021**, *216*, 109066.

[10] a) L. F. Zhu, Y. Z. Chen, W. H. Shang, S. Handschuh-Wang, X. H. Zhou, T. S. Gan, Q. X. Wu, Y. Z. Liu, X. C. Zhou, *J. Mater. Chem. C* **2019**, *7*, 10166; b) T. V. Neumann, E. G. Facchine, B. Leonardo, S. Khan, M. D. Dickey, *Soft Matter* **2020**, *16*, 6608; c) H. Wang, Y. Yao, Z. He, W. Rao, L. Hu, S. Chen, J. Lin, J. Gao, P. Zhang, X. Sun, X. Wang, Y. Cui, Q. Wang, S. Dong, G. Chen, J. Liu, *Adv. Mater.* **2019**, *31*, 1901337; d) H. Z. Liu, Y. M. Xin, Y. Lou, Y. Peng, L. L. Wei, J. Y. Zhang, *Mater. Horiz.s* **2020**, *7*, 2141.

[11] a) S. Q. Li, Q. Liu, Z. J. Sun, Q. Y. Liu, A. Lv, Z. K. Hu, Y. T. Xu, S. S. Wan, H. L. Hu, Z. H. Liu, X. D. Fu, Q. T. Liu, S. F. Hu, R. Zhang, C. P. Wong, *Compos. Sci. Technol.* **2021**, *216*, 109037; b) A. Mohammadi Nasab, T. L. Buckner, B. Yang, R. Kramer-Bottiglio, *Adv. Mater. Technol.* **2021**, *7*, 2100920; c) A. Koh, J. Sietins, G. Slipher, R. Mrozek, *J. Mater. Res.* **2018**, *33*, 2443.

[12] a) Y. S. Han, L. E. Simonsen, M. H. Malakooti, *Adv. Energy Mater.* **2022**, *12*, 2201413; b) T. V. Neumann, M. D. Dickey, *Adv. Mater. Technol.* **2020**, *5*, 2000070.

[13] a) A. Hajalilou, A. F. Silva, P. A. Lopes, E. Parvini, C. Majidi, M. Tavakoli, *Adv. Mater. Interfaces* **2022**, *9*, 2101913; b) E. J. Barron, 3rd, R. S. Peterson, N. Lazarus, M. D. Bartlett, *ACS Appl. Mater. Interfaces* **2020**, *12*, 50909.

[14] a) Y. Sargolzaeiaval, V. P. Ramesh, T. V. Neumann, R. Miles, M. D. Dickey, M. C. Ozturk, *ECS J. Solid State Sci. Technol.* **2019**, *8*, P357; b) M. G. Saborio, S. Cai, J. Tang, M. B. Ghasemian, M. Mayyas, J. Han, M. J. Christoe, S. Peng, P. Koshy, D. Esrafilzadeh, R. Jalili, C. H. Wang, K. Kalantar-Zadeh, *Small* **2020**, *16*, 1903753.

[15] a) C. Li, H. Y. Chen, L. Zhang, J. Zhong, *AIP Adv.* **2020**, *10*, 105106; b) M. G. Kim, B. Lee, M. Li, S. Noda, C. Kim, J. Kim, W. J. Song, S. W. Lee, O. Brand, *ACS Nano* **2020**, *14*, 5659; c) J. B. Dou, L. X. Tang, L. Mou, R. F. Zhang, X. Y. Jiang, *Compos. Sci. Technol.* **2020**, *197*, 108237.

[16] E. J. Krings, H. Zhang, S. Sarin, J. E. Shield, S. Ryu, E. J. Markvicka, *Small* **2021**, *17*, 2104762.

[17] C. Pan, E. J. Markvicka, M. H. Malakooti, J. Yan, L. Hu, K. Matyjaszewski, C. Majidi, *Adv. Mater.* **2019**, *31*, 1900663.

[18] M. Wang, K. Zhang, X. X. Dai, Y. Li, J. Guo, H. Liu, G. H. Li, Y. J. Tan, J. B. Zeng, Z. Guo, *Nanoscale* **2017**, *9*, 11017.

[19] S. F. Mei, Y. X. Gao, Z. S. Deng, J. Liu, *J. Electron. Packag.* **2014**, *136*, 7.

[20] Y. Peng, H. Z. Liu, Y. M. Xin, J. Y. Zhang, *Matter* **2021**, *4*, 3001.

[21] L. Sanchez-Botero, D. S. Shah, R. Kramer-Bottiglio, *Adv. Mater.* **2022**, *34*, 2109427.

[22] L. Tang, S. Cheng, L. Zhang, H. Mi, L. Mou, S. Yang, Z. Huang, X. Shi, X. Jiang, *iScience* **2018**, *4*, 302.

[23] R. Tutika, S. Kmiec, A. Haque, S. W. Martin, M. D. Bartlett, *ACS Appl. Mater. Interfaces* **2019**, *11*, 17873.

[24] Z. Nie, J. W. Kwak, M. Han, J. A. Rogers, *Adv. Mater.* **2022**, 2205609.

[25] S. H. Jeong, S. Chen, J. Huo, E. K. Gamstedt, J. Liu, S. L. Zhang, Z. B. Zhang, K. Hjort, Z. Wu, *Sci. Rep.* **2015**, *5*, 18257.